Received July 17, 2019, accepted July 18, 2019, date of publication July 22, 2019, date of current version August 9, 2019.

Digital Object Identifier 10.1109/ACCESS.2019.2930333

Multicarrier Division Duplex Aided Millimeter Wave Communications

RAKSHITH RAJASHEKAR[1], (Senior Member, IEEE), CHAO XU[1], (Member, IEEE), NAOKI ISHIKAWA[2], (Member, IEEE), LIE-LIANG YANG[1], (Fellow, IEEE), AND LAJOS HANZO[1], (Fellow, IEEE)

[1]School of Electronics and Computer Science, University of Southampton, Southampton SO17 1BJ, U.K.
[2]Graduate School of Information Sciences, Hiroshima City University, Hiroshima 731-3194, Japan

Corresponding author: Lajos Hanzo (lh@soton.ac.uk)

This work was supported in part by the EPSRC under Project EP/Noo4558/1 and Project EP/PO34284/1, in part by the European Research Council's Advanced Fellow Grant under the QuantCom project, in part by the Royal Society's Wolfson Research Merit Award, and in part by the Royasl Society's Global Research Challenges Fund. The work of N. Ishikawa was supported in part by the Japan Society for the Promotion of Science KAKENHI under Grant 17H07036. The research data supporting this paper can be obtained from University of Southampton repository https://doi.org/10.5258/SOTON/D1021.

ABSTRACT The existing time-division duplex (TDD) and frequency-division duplex (FDD) techniques rely on a guard time and/or a guard band to avoid self-interference (SI) between the uplink and downlink channels, which results in the wastage of precious spectral resources. The full-duplex (FD) schemes of in-band FD (IBFD), as well as multicarrier division duplex (MDD), may overcome this drawback while retaining the key benefits of both TDD and FDD. Moreover, the MDD exhibits the exclusive benefits of the reduced peak-to-average-power ratio (PAPR) for signal transmission as well as the SI-free signal detection. Against this background, in this paper, we propose a novel FD scheme conceived for frequency-selective millimeter-wave (mmWave) channels, which have not been investigated in the open literature. Furthermore, we propose a novel projection-aided iterative eigenvalue decomposition (P-IEVD) algorithm, which performs null-space SI cancellation in the inherent beamforming structure of mmWave communication. Our simulation results confirm that the MDD is capable of outperforming its half-duplex (HD) counterparts of the TDD/FDD, even the IBFD can only achieve a better bandwidth efficiency than the MDD when a sufficiently high SNR is provided.

INDEX TERMS Full duplex, orthogonal frequency division multiplexing, millimeter wave, uniform linear array, multicarrier division duplex, analog-to-digital converter dynamic range, power-amplifier dynamic range, beamforming, nullspace self-interference cancellation, dynamic subcarrier allocation.

I. INTRODUCTION

Time Division Duplex (TDD) and Frequency Division Duplex (FDD) [1]–[4] have been the dominant spectrum access techniques both in the IEEE 802.11a/n/ac/ah family as well as in the emerging 5G cellular network. Recently, the Full-Duplex (FD) techniques including the In-Band Full Duplex (IBFD) [5]–[11] and Multicarrier Division Duplex (MDD) [12]–[17], which are capable of better exploiting the valuable spectral resources, have attracted substantial interest both in academia and in the wireless industry. The schematics of these basic access techniques are portrayed in Fig. 1, and their features are summarized in Table 2, where the advantages are highlighted in blue.

First of all, the TDD separates the Up Link (UL) and Down Link (DL) in the time domain, where a guard interval is required, as shown in Fig. 1 for accommodating the transients between the switching instants. On one hand, the TDD mode is known to have three main advantages, as highlighted in Table 2. Firstly, as a benefit of the combined UL and DL spectrum, both links can access to the entire allotted channel bandwidth, which improves the frequency diversity. Secondly, thanks to channel reciprocity, the Channel State Information at the Transmitter (CSIT) is available without feedback. This is beneficial both for beamforming and resource allocation. Thirdly, the TDD mode is capable of supporting asymmetric traffic by appropriately

The associate editor coordinating the review of this manuscript and approving it for publication was Derek Abbott.

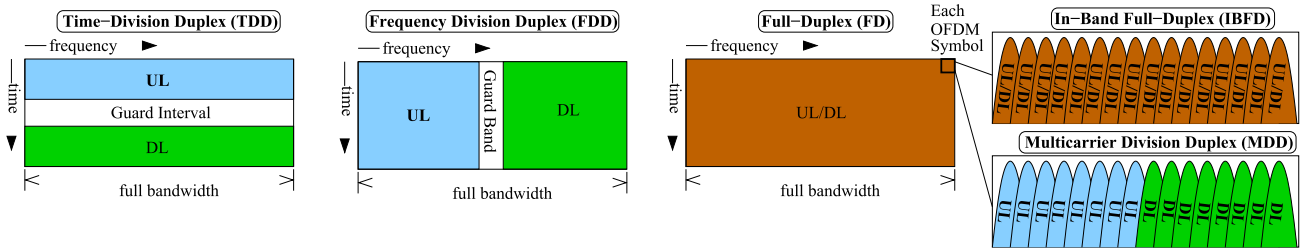

FIGURE 1. Schematic descriptions of Time Division Duplex (TDD), Frequency Division Duplex (FDD), In-Band Full-Duplex (IBFD) and Multicarrier Division Duplex (MDD).

TABLE 1. Nomenclature.

ADC	Analog-to-Digital Converter
AoA	Angle of Arrival
AoD	Angle of Departure
AP	Access Point
BS	Base Station
CSI	Channel State Information
CSIT	Channel State Information at Transmitter
DAC	Digital-to-Analog Converter
DFT	Discrete Fourier Transform
DL	Down Link
FD	Full Duplex
FDD	Frequency Division Duplex
FSPL	Free-Space Path Loss
HARQ	Hybrid Automatic Repeat reQuest
HD	Half Duplex
IBFD	In-Band Full Duplex
IDFT	Inversed Discrete Fourier Transform
IEVD	Iterative Eigenvalue Decomposition
LoS	Line-of-Sight
LTE	Long-Term Evolution
M2M	Multipoint-to-Multipoint
MAC	Medium Access Control
MDD	Multicarrier Division Duplex
MPC	Multi-Path Component
MS	Mobile Station
NLoS	Non Line-of-Sight
NR	New Radio
OFDM	Orthogonal Frequency Division Multiplexing
P2P	Point-to-Point
PA	Power Amplifier
PAPR	Peak-to-Average Power Ratio
P-IEVD	Projection based Iterative Eigenvalue Decomposition
RA	Receive Antenna
Rx	Receiver
SI	Self-Interference
SIQNR	Self-Interference-to-Quantization Noise power Ratio
SQNR	Signal-to-Quantization Noise power Ratio
TA	Transmit Antenna
TDD	The Time Division Duplex
Tx	Transmitter
UL	Up Link
ULA	Uniform Linear Array

apportioning the UL and DL durations. However, TDD also suffers from three disadvantages, which are also summarized in Table 2. Firstly, the TDD guard interval has to take into account the round-trip delays of the cell-edge mobile users. The associated stringent time synchronization inevitably limits the cell radius. Secondly, the hidden terminal problem arises, when the carrier sensing initiated by Node 1 falsely detects an idle state of the Access Point (AP), which is not transmitting but receiving from Node 2 that appears to

TABLE 2. Comparison of access technologies (their advantages are highlighted in blue).

	TDD	FDD	IBFD	MDD
Guard interval	Required	None	None	None
UL/DL spectrum	Combined	Separated	Combined	Combined
CSIT (shared Tx/Rx antennas)	Channel reciprocity	Require feedback	Channel reciprocity	Channel reciprocity
Asymmetric traffic	Flexible	Symmetric	Symmetric	Flexible
Guard band	None	Required	None	None
Synchronization	Required	None	Required	Required
Hidden terminal	Exist	Avoided	Avoided	Avoided
Delayed HARQ	Delayed	Avoided	Avoided	Avoided
Bandwidth efficiency	Classic	Classic	Improved	Improved
OFDM PAPR	Classic	Classic	Classic	Reduced
SI (signal reception)	None	None	Exist	Exist
SI (signal detection)	None	None	Exist	None

be hidden to Node 1 [5]. Thirdly, due to the TDD delay, the CSIT may become outdated, which may be further aggravated by Hybrid Automatic Repeat reQuest (HARQ) in the Medium Access Control (MAC) layer. Nonetheless, in the most up-to-date 5G New Radio (NR) standard releases [18], TDD is the sole access technology adopted both in the C-band (4 GHz–5 GHz) as well as in the mmWave K-band (24 GHz–27 GHz) and Ka-band (27 GHz–40 GHz). Moreover, TDD also coexists with the FDD mode both in the L-band (1 GHz–2 GHz) and in the S-band (2 GHz–4 GHz).

As an out-of-band full-duplex scheme, the FDD mode concurrently transmits and receives signals at separate frequencies, as portrayed in Fig. 1. On one hand, the FDD mode may efficiently alleviate the aforementioned TDD disadvantages of stringent time synchronization, hidden terminal problem and delayed HARQ, as seen in Table 2. On the other hand, a sufficiently wide guard band is required for the sake of avoiding power leakage between the UL and DL, which results in a waste of the valuable spectral resources. Moreover, the FDD mode is inflexible in terms of supporting asymmetric traffics. All these features render the FDD mode suitable for long-range symmetric and low-rate communications in the low-frequency microwave bands. In the 5G NR standard releases [18], the FDD mode is deployed in the Ultra High Frequency (UHF) band (0.3 GHz–1 GHz), L-band (1 GHz–2 GHz) as well as in the lower half of the S-band (2 GHz–3 GHz), which are inherited from the legacy microwave 2G-4G cellular networks.

By contrast, the IBFD scheme aims for simultaneously transmitting and receiving signals in the same band, which

may potentially make the spectral resources twice as valuable, as demonstrated in Fig. 1. According to fundamental antenna theory, the electromagnetic fields of the transmitted and received signals are independent of each other [19], hence the IBFD mode has already been widely implemented in continuous-wave radar systems since the 1940s [9]. As the benefit of simultaneous signal transmission and reception, the IBFD is capable of improving the bandwidth efficiency, while both the TDD problems of guard interval, hidden terminal and delayed HARQ as well as the FDD problems of guard band, feedback for CSIT and inflexibility in asymmetric traffic are all effectively eliminated [5]–[11], as presented in Table 2.

However, the major challenge in IBFD is the strong Self-Interference (SI) that is leaked from the transmitter to the receiver of the same node. Intuitively, the full-duplex node knows its transmitted signal, which should be directly subtracted from the received signal without causing SI. However, the SI that received from its own transmitter may be up to billions time stronger than the signal received from the desired transmitting node (30-120 dB [6], [8]–[11]). As a result, the finite-precision Analog-to-Digital Converter (ADC) is often saturated by the SI, which imposes overwhelming quantization noise to the desired signal. For example, let us assume that the SI is 40 dB (=10000 times) stronger than the desired received signal. Based on the rule-of-thumb ADC dynamic range of $6.02Q$ dB, where Q denotes the number of ADC resolution bits, a dynamic range of 48.2 dB is provided by the ADC for $Q = 8$ bits. However, owing to the strong SI of 40 dB that saturates most of the ADC dynamic range, the effective ADC dynamic range left for the desired signal is reduced to $48.2 - 40 = 8.2$ dB, which corresponds to merely $8.2/6.02 \approx 1.36$ ADC resolution bits. This detrimental effect inevitably results in a substantially increased quantization noise to the desired signal.

In general, the SI in the IBFD scheme has to be mitigated for both signal reception in analog domain and signal detection in digital domain [9]–[11], as shown in Table 2. As the frontier defense mechanism against SI, the transmit and receive antennas are often separated in the propagation domain, where the physical distance, the blocking obstacles and careful antenna placement may attenuate the SI. As the second line of defense, the SI has to be modeled and subtracted from the received signal by the analog circuitry before ADC, which improves the signal reception. Finally, the residual SI after ADC is further mitigated in the digital domain, which improves the signal detection. In summary, all the aforementioned SI mitigation techniques inevitably impose extra hardware and software costs and constraints, which impede their implementation in commercial networks.

The MDD [12]–[17] is capable of overcoming some of the drawbacks of the aforementioned access techniques without compromising their key benefits. Specifically, the MDD assigns orthogonal subcarriers in each Orthogonal Frequency Division Multiplexing (OFDM) symbol to the separate UL and DL channels, as demonstrated in Fig. 1. As a result, the MDD has the following advantages, as summarized in Table 2:

(A.1) Owing to the orthogonal OFDM subcarrier division shown in Fig. 1, the MDD is completely free of SI during the signal detection in the digital domain.

(A.2) Since only a fraction of the OFDM subcarriers are activated for the UL and DL, the Peak-to-Average Power Ratio (PAPR) of the transmitted signals is substantially reduced. The associated power consumption reduction for the Power Amplifier (PA) is achieved without the extra complexity of invoking any of the conventional PAPR reduction techniques, such as active constellation extension, selected mapping, tone injection and tone reservation [20]–[23].

(A.3) In the face of asymmetric UL/DL traffic, the MDD is capable of dynamically assigning a smaller portion of OFDM subcarriers to the lower-traffic UL, which in turn reduces the power consumption for the shirt-pocket-sized MSs having a compact form-factor.

(A.4) The MDD retains the IBFD advantages of eliminating the guard interval/band, acquiring CSIT without feedback, instantaneous HARQ and avoiding the hidden terminal problem.

Nonetheless, we will demonstrate in this paper that the tradeoff between IBFD and MDD is very similar to the tradeoff between FDD and TDD, where IBFD outperforms MDD at sufficiently high SNRs. More explicitly, the inherent disadvantages of MDD seen in Table 2 are summarized as follows:

(D.1) Despite its beneficial SI-free nature in the digital domain, the effect of SI on the dynamic range of the ADC used for signal reception still has to be addressed in the MDD regime.

(D.2) As a result of the separate subcarrier assignments for the UL and DL, the overall system throughput of MDD cannot compete with IBFD. Nonetheless, we will demonstrate that due to the residual SI contaminating the signal detection, the IBFD can only achieve a higher bandwidth efficiency, when a sufficiently high SNR is provided.

(D.3) Owing to the simultaneous signal transmission and reception, both MDD and IBFD impose stringent requirements on time synchronization. Moreover, all of the OFDM-based duplex techniques of TDD, FDD, IBFD and MDD suffer from a phase noise that increases with the oscillator's carrier frequency, which has to be dealt with by the Phase-Tracking Reference Signal (PT-RS) in the most up-to-date 5G standards [24].

Against this background, the contributions of this paper are explicitly summarized as follows:

1) In this work, we propose a novel FD-based bidirectional Point-to-Point (P2P) transmission scheme for frequency-selective mmWave channels, which has not been investigated in the open literature. More explicitly, first of all, the duplex Transmitter (Tx) and

Receiver (Rx) are modeled by Uniform Linear Arrays (ULAs) associated with adjustable separation distance and angle parameters, which subsumes the special case of Tx and Rx sharing the same antenna array. Secondly, we model the Line-of-Sight (LoS) SI channels by the near-field propagation model, which allows us to perform tractable analysis. Thirdly, the Non-Line-of-Sight (NLoS) SI channels as well as the multipath communication channels between the two nodes are modeled by the far-field propagation model, where the sparsity of both the spatial and time domains are exploited.

2) Without loss of generality, we propose to mitigate the LoS SI by nullspace cancelling in the inherent beamforming structure of mmWave communication. To elaborate, in addition to the objective of maximizing the beamforming gain, an extra constraint of creating null beams for the LoS SI channels is added in the FD mode. As a result, although the Half-Duplex (HD) TDD scheme is capable of achieving a higher beamforming gain in the absence of any SI mitigation constraint, our simulation results confirm that the FD schemes of IBFD and MDD consistently exhibit higher bandwidth efficiencies than their HD TDD counterparts.
3) The comparison between the FD scheme pair of MDD and IBFD is examined in terms of the following three aspects. First of all, regarding the Tx PA dynamic range required for signal transmission, the MDD exhibits substantially reduced PAPR, which reduces the power consumption at the Tx. Secondly, in terms of signal reception, both MDD and IBFD have to take into account the ADC dynamic range in the context of the proposed nullspace SI cancellation. Thirdly, owing to the fact that the OFDM subcarriers are separately assigned to the bidirectional links, ''clean'' uncontaminated received signals without SI become available to the MDD in the digital domain. As a result, our simulation results demonstrate that the MDD is capable of outperforming the IBFD in small mmWave cells, unless unrealistically high SNRs are assumed.

The remainder of the paper is organized as follows. The MDD aided P2P mmWave communication system as well as the associated SI and the mmWave channel models are presented in Section II. The issues of the PA dynamic range and the effective ADC bitwidth reduction as well as our beamforming aided solution are presented in Section III. Our simulation studies are presented in Section IV, while Section V concludes the paper.

II. MDD AIDED mm-WAVE COMMUNICATION SYSTEM

A. SYSTEM MODEL

Let us consider a pair of MDD nodes communicating with each other, as shown in Fig. 2. Each node is assumed to have N_{ti} Transmit Antennas (TAs) and N_{ri} Receive Antennas (RAs) placed in a Uniform Linear Array (ULA) with half-wavelength spacing, where i denotes the index of the node. Each antenna chain is assumed to be followed/preceded

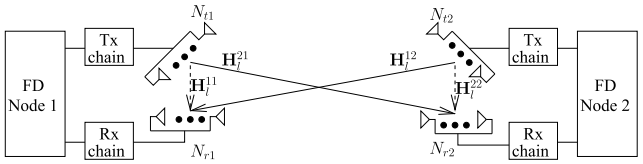

FIGURE 2. Notations of Full-Duplex (FD) aided bidirectional Point-to-Point (P2P) mmWave communication system.

by a variable gain amplifier and a phase shifter, which are used for employing transmit as well as receive beamforming. Furthermore, let $\mathbf{w}_{ti} \in \mathbb{C}^{N_{ti}}$ and $\mathbf{w}_{ri} \in \mathbb{C}^{N_{ri}}$ represent the unit-norm transmit and receive beamforming vectors at node i. The signal sequence received at the i^{th} node is given by:

$$r_i(n) = \sqrt{\rho_{ij}} \sum_{l=0}^{N_c-1} \mathbf{w}_{ri}^H \mathbf{H}_l^{ij} \mathbf{w}_{tj} x_j(n - m_l^{ij}) + \underbrace{\sqrt{\rho_{ii}^{\text{LoS}}} \mathbf{w}_{ri}^H \mathbf{H}_0^{ii} \mathbf{w}_{ti} x_i(n - m_0^{ii})}_{\text{LoS SI}} + \underbrace{\sqrt{\rho_{ii}} \sum_{l=1}^{N_c-1} \mathbf{w}_{ri}^H \mathbf{H}_l^{ii} \mathbf{w}_{ti} x_i(n - m_l^{ii})}_{\text{NLoS SI}} + z(n), \quad (1)$$

where N_c is the number of multipath clusters, $\mathbf{H}_l^{ij} \in \mathbb{C}^{N_{ri} \times N_{tj}}$ represents the channel matrix corresponding to the l^{th} multipath cluster between the j^{th} transmitter and the i^{th} receiver, $\mathbf{H}_0^{ii}$ represents the strongest LoS SI channel at the i^{th} node, $\mathbf{H}_l^{ii}$ represent the NLoS multipath components associated with the SI channel at the i^{th} node, m_l^{ij} is the multipath delay associated with $\mathbf{H}_l^{ij}$, $x_i(n)$ is the data sequence transmitted by node i, and $z(n) \sim \mathcal{CN}(0, \sigma^2)$[1] is the thermal noise. Owing to the physical separation between the transmit and receive antennas, the NLoS SI component of (1) is modeled in the same way as the desired channel's frequency-selective multipath propagation link between the two nodes, where the distribution of the multipath channels $\mathbf{H}_l^{ij}$ and $\mathbf{H}_l^{ii}$ as well as that of their delays m_l^{ij} and m_l^{ii} will be introduced in Sec. II-B. We note that this does not impose any problem on the bespoke OFDM scheme considered in this work, as long as the cyclic prefix is longer than the maximum delay D.

For the sake of clarity, (1) may be simplified as:

$$r_i(n) = \sqrt{\rho_{ij}} \sum_{l=0}^{N_c-1} \overline{h}_l^{ij} x_j(n - m_l^{ij}) + \underbrace{\sqrt{\rho_{ii}^{\text{LoS}}} \overline{h}_0^{ii} x_i(n - m_0^{ii})}_{\text{LoS SI}} + \underbrace{\sqrt{\rho_{ii}} \sum_{l=1}^{N_c-1} \overline{h}_l^{ii} x_i(n - m_l^{ii})}_{\text{NLoS SI}} + z(n), \quad (2)$$

[1]The complex Gaussian random variable with mean μ and variance σ^2 is represented by $\mathcal{CN}(\mu, \sigma^2)$.

where $\{\bar{h}_l^{ij} = \mathbf{w}_{ri}^H \mathbf{H}_l^{ij} \mathbf{w}_{tj}\}_{l=0}^{N_c-1}$ and $\{\bar{h}_l^{ii} = \mathbf{w}_{ri}^H \mathbf{H}_l^{ii} \mathbf{w}_{ti}\}_{l=0}^{N_c-1}$ denote the beamformed channels.

B. CHANNEL MODEL

In recent years, substantial research efforts have been dedicated to beamforming design [25]–[37] that takes into account both channel estimation [27]–[29], and multi-user access [30]–[33] as well as full-duplex scenarios [34]–[37] in the *narrowband* mmWave channels. However, the mmWave mode of the most recent 5G New Radio (NR) standard releases is OFDM-based [24]. Against this background, in this work, we invoke the following frequency-selective mmWave channel model [38], [39] for (1) that subsumes all the aforementioned narrowband models as a special case:

$$\mathbf{H}^{ij}(m) = \sum_{l=0}^{N_c-1} \mathbf{H}_l^{ij} \delta(m - m_l^{ij}). \tag{3}$$

The multipath delays m_l^{ij} are assumed to be uniformly distributed over $[0, 1, \ldots, D]$, where D corresponds to the largest multipath delay. We define $m_0^{ij} \neq m_1^{ij} \neq \cdots \neq m_{N_c-1}^{ij}$ and $N_c < D$, owing to the fact that mmWave channel has limited scattering. Furthermore, since the distance between the two nodes is far larger than the mmWave wavelength, the multipath cluster in (3) is further extended according to the far-field propagation model [37], [40], [40] as:

$$\mathbf{H}_l^{ij} = \sqrt{\frac{N_{tj} N_{ri}}{N_c}} \sum_{k=0}^{N_{ray}-1} \alpha_k^l \mathbf{e}_{ri}(\theta_k^l) \mathbf{e}_{tj}^H(\phi_k^l), \tag{4}$$

where N_{ray} is the number of Multi-Path Components (MPCs), while each MPC $\alpha_k^l \sim \mathcal{CN}(0, 1)$ has independent Angle of Arrival (AoA) θ^l and Angle of Departure (AoD) ϕ_k^l. These angles θ_k^l and ϕ_k^l are generated using Laplacian distribution with mean values of $\bar{\theta}^l$ and $\bar{\phi}^l$, variances of σ_θ^2 and σ_ϕ^2, respectively, where $\bar{\theta}^l$ and $\bar{\phi}^l$ are assumed to be uniformly distributed in the interval $[0, 2\pi)$. Moreover, the array response vectors of the i^{th} receiver's and j^{th} transmitter's ULAs are given by:

$$\begin{aligned} \mathbf{e}_{ri}(\theta_k^l) &= \frac{1}{\sqrt{N_{ri}}} \left[e^{j\pi 0\theta_k^l} \; e^{j\pi 1\theta_k^l} \; \cdots \; e^{j\pi(N_{ri}-1)\theta_k^l} \right], \\ \mathbf{e}_{tj}(\phi_k^l) &= \frac{1}{\sqrt{N_{tj}}} \left[e^{j\pi 0\phi_k^l} \; e^{j\pi 1\phi_k^l} \; \cdots \; e^{j\pi(N_{tj}-1)\phi_k^l} \right]. \end{aligned} \tag{5}$$

The LoS component of the SI channel depends on the geometries of the transmit and receive ULAs. Assuming that the transmit and receive ULAs are separated by a distance d and have an angular inclination of ϑ, as portrayed by Fig. 3, the LoS SI in (1) is represented by the near-field propagation model [41]–[43] as:

$$\mathbf{H}_0^{ii}(q, p) = \frac{\xi}{d_{qp}} e^{-j\frac{2\pi}{\lambda} d_{qp}}, \tag{6}$$

where ξ is the power normalization constant ensuring that we have $\mathsf{trace}(\mathbf{H}_0^{ii} \mathbf{H}_0^{iiH}) = N_{ti} N_{ri}$, while the distance between the p^{th} TA and q^{th} RA is given by (7), as shown at the bottom of this page.

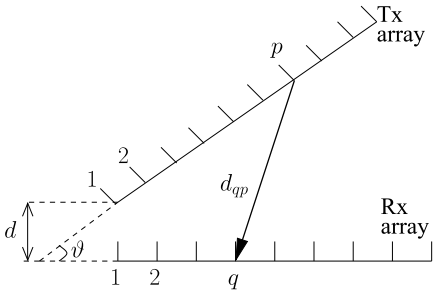

FIGURE 3. Pictorial depiction of the transmit and receive antenna array geometry at each node.

We note that the pair of transmit and receive ULAs deployed at the same node seen in Fig. 3 are configured in a two-dimensional plane, since no relative transmitter-receiver movement is considered. The readers may refer to [44] for the practical three-dimensional deployment, where the effect of polarization mismatch between the transmit and receive ULAs located at two separate nodes is taken into account.

Moreover, for the special case of Tx and Rx sharing the same array, we have $d = 0$ and $\vartheta = 0$. In this case, however, the extra hardware cost of either a three-point circulator or an electrical balance duplexer has to be equipped for each antenna element, so that the flow of transmit and receive signals is directed in a clockwise manner [9]–[11]. However, the antenna separation aided scenario of $d > 0$ and $\vartheta > 0$ inevitably complicates the CSIT acquisition for both IBFD and MDD. Nonetheless, thanks to the combined UL/DL spectrum, the channel reciprocity seen in Table 2 is still valid during the stage of channel sounding phase invoked for resource scheduling, since practical mmWave communications do not always activate all antennas over the entire available spectrum for each link. In the most up-to-date 5G standards, the grant-based resource scheduling and beam selection are assisted by the Sounding Reference Signal (SRS) and CSI Reference Signal (CSI-RS), which are independent of the Demodulation Reference Signal (DM-RS) used for the accurate estimation of the amplitudes and phases of the Channel Impulse Responses (CIRs) for the sake of performing coherent detection [24].

$$d_{qp} = \sqrt{\left[\frac{d}{\tan\vartheta} + \frac{(q-1)\lambda}{2}\right]^2 + \left[\frac{d}{\sin\vartheta} + \frac{(p-1)\lambda}{2}\right]^2 - 2\left[\frac{d}{\tan\vartheta} + \frac{(q-1)\lambda}{2}\right]\left[\frac{d}{\sin\vartheta} + \frac{(p-1)\lambda}{2}\right]\cos\vartheta} \tag{7}$$

Finally, similar to (3), the NLoS SI of (1) is given by:

$$\mathbf{H}^{ii}(m) = \sum_{l=1}^{N_c-1} \mathbf{H}_l^{ii}\delta(m - m_l^{ii}), \tag{8}$$

where the MPCs $\mathbf{H}_l^{ii}$ are also generated according to the far-field model of (4).

C. OFDM MODEL

For an OFDM system having N subcarriers, the time-domain samples in (1)-(2) are generated by the Inversed Discrete Fourier Transform (IDFT) as $x_i(n) = \frac{1}{\sqrt{N}}\sum_{\kappa=0}^{N-1} s_i(\kappa)w_N^{\kappa n}$ and $x_j(n) = \frac{1}{\sqrt{N}}\sum_{\kappa=0}^{N-1} s_j(\kappa)w_N^{\kappa n}$, where $\{s_i(\kappa)\}_{\kappa=0}^{N-1}$ and $\{s_j(\kappa)\}_{\kappa=0}^{N-1}$ are the OFDM symbols modulated at the i^{th} and j^{th} node, respectively, while we have $w_N = \exp(j\frac{2\pi}{N})$. The IDFT may be expressed in matrix form as $\mathbf{x}_i = \mathbf{W}_N^H\mathbf{s}_i$ and $\mathbf{x}_j = \mathbf{W}_N^H\mathbf{s}_j$, where $\mathbf{W}_N \in \mathbb{C}^{N\times N}$ is the Discrete Fourier Transform (DFT) matrix, while we have the frequency-domain vectors $\mathbf{s}_i \in \mathbb{C}^N$ and $\mathbf{s}_j \in \mathbb{C}^N$ and the time-domain vectors $\mathbf{x}_i \in \mathbb{C}^N$ and $\mathbf{x}_j \in \mathbb{C}^N$.

In the OFDM model, the received samples of (2) may be formulated as:

$$r_i(n) = \sqrt{\rho_{ij}}\sum_{l_d=0}^{D}\widetilde{h}_{l_d}^{ij}x_j\langle n-l_d\rangle_N + \sqrt{\rho_{ii}}\sum_{l_d=0}^{D}\widetilde{h}_{l_d}^{ii}x_i\langle n-l_d\rangle_N + z(n), \tag{9}$$

where $\langle n-l_d\rangle_N$ denotes $(n-l_d)$ modulo N, while the sparse delayed and beamformed channels are given by:

$$\widetilde{h}_{l_d}^{ij} = \begin{cases}\bar{h}_l^{ij} = \mathbf{w}_{ri}^H\mathbf{H}_l^{ij}\mathbf{w}_{tj}, & \text{if } l_d = m_l^{ij}\\ 0, & \text{otherwise,}\end{cases}$$
$$\widetilde{h}_{l_d}^{ii} = \begin{cases}\bar{h}_l^{ii} = \mathbf{w}_{ri}^H\mathbf{H}_l^{ii}\mathbf{w}_{ti}, & \text{if } l_d = m_l^{ii}\\ 0, & \text{otherwise.}\end{cases} \tag{10}$$

As a result, (9) may be expressed in matrix form for the N-subcarrier OFDM system as:

$$\mathbf{r}_i = \sqrt{\rho_{ij}}\widetilde{\mathbf{H}}^{ij}\mathbf{x}_j + \sqrt{\rho_{ii}}\widetilde{\mathbf{H}}^{ii}\mathbf{x}_i + \mathbf{z}, \tag{11}$$

where $\widetilde{\mathbf{H}}^{ij} \in \mathbb{C}^{N\times N}$ and $\widetilde{\mathbf{H}}^{ii} \in \mathbb{C}^{N\times N}$ are circulant matrices associated with $\{\widetilde{h}_{l_d}^{ij}\}_{l_d=0}^{D}$ and $\{\widetilde{h}_{l_d}^{ii}\}_{l_d=0}^{D}$, respectively.

Finally, the frequency-domain received OFDM symbol after DFT is given by:

$$\mathbf{y}_i = \mathbf{W}_N\mathbf{r}_i = \sqrt{\rho_{ij}}\mathbf{D}^{ij}\mathbf{s}_j + \sqrt{\rho_{ii}}\mathbf{D}^{ii}\mathbf{s}_i + \check{\mathbf{z}}, \tag{12}$$

where $\mathbf{D}^{ij} = \mathbf{W}_N\widetilde{\mathbf{H}}^{ij}\mathbf{W}_N^H$ and $\mathbf{D}^{ii} = \mathbf{W}_N\widetilde{\mathbf{H}}^{ii}\mathbf{W}_N^H$ are the diagonal matrices having channel coefficients in the Fourier-domain, while we have $\check{\mathbf{z}} = \mathbf{W}_N\mathbf{z}$.

D. MDD AND IBFD

In this work, we focus our attention on the bidirectional P2P system of Fig. 2 associated with symmetric traffic. Therefore, the MDD subcarrier allocation within an OFDM symbol may be expressed as:

$$\begin{cases}s_i(\kappa) \neq 0 \text{ and } s_j(\kappa) = 0, & 0 \le \kappa \le N/2-1\\ s_i(\kappa) = 0 \text{ and } s_j(\kappa) \neq 0, & N/2 \le \kappa \le N-1.\end{cases} \tag{13}$$

Moreover, in the case of dynamic subcarrier allocation based on the link qualities, the MDD transmission may be optimized as:

$$\begin{cases}s_i(\kappa) \neq 0 \text{ and } s_j(\kappa) = 0, & \text{if } |\mathbf{D}^{ji}(\kappa,\kappa)| > |\mathbf{D}^{ij}(\kappa,\kappa)|\\ s_i(\kappa) = 0 \text{ and } s_j(\kappa) \neq 0, & \text{otherwise.}\end{cases} \tag{14}$$

As a result, the MDD signal detection in the digital domain is "clean" and completely free from SI, where (12) is extended as:

$$\begin{cases}y_i(\kappa) = \sqrt{\rho_{ij}}\mathbf{D}^{ij}(\kappa,\kappa)s_j(\kappa) + \check{\mathbf{z}}(\kappa), & \text{if } s_j(\kappa) \neq 0\\ y_j(\kappa) = \sqrt{\rho_{ji}}\mathbf{D}^{ji}(\kappa,\kappa)s_i(\kappa) + \check{\mathbf{z}}(\kappa), & \text{if } s_i(\kappa) \neq 0.\end{cases} \tag{15}$$

Consequently, the MDD bandwidth efficiencies achieved at Node 1 and Node 2 of Fig. 2 are given by:

$$C_{\text{MDD}}^{\text{Node1}} = \frac{2}{N}E\{\sum\nolimits_{\forall s_2(\kappa)\neq 0}\log_2\left[1+\rho_{12}|\mathbf{D}^{12}(\kappa,\kappa)|^2\right],$$
$$C_{\text{MDD}}^{\text{Node2}} = \frac{2}{N}E\{\sum\nolimits_{\forall s_1(\kappa)\neq 0}\log_2\left[1+\rho_{21}|\mathbf{D}^{21}(\kappa,\kappa)|^2\right]. \tag{16}$$

In summary, the MDD activates half of the OFDM subcarriers for each link so that the signal detection becomes SI-free.

By contrast, the IBFD always activates all OFDM subcarriers for each link as:

$$s_i(\kappa) \neq 0 \text{ and } s_j(\kappa) \neq 0, \quad 0 \le \kappa \le N-1. \tag{17}$$

Therefore, the IBFD bandwidth efficiency of each node may be evaluated based on (12) as:

$$C_{\text{IBFD}}^{\text{Node1}} = \frac{1}{N}E\{\sum\nolimits_{\kappa=0}^{N-1}\log_2\left[1+\frac{\rho_{12}|\mathbf{D}^{12}(\kappa,\kappa)|^2}{1+\rho_{11}|\mathbf{D}^{11}(\kappa,\kappa)|^2}\right]\},$$
$$C_{\text{IBFD}}^{\text{Node2}} = \frac{1}{N}E\{\sum\nolimits_{\kappa=0}^{N-1}\log_2\left[1+\frac{\rho_{21}|\mathbf{D}^{21}(\kappa,\kappa)|^2}{1+\rho_{22}|\mathbf{D}^{22}(\kappa,\kappa)|^2}\right]\}. \tag{18}$$

Intuitively, the IBFD achieves an improved throughput, since all of the N OFDM subcarriers are activated for each link. However, compared to the MDD of (16), the performance of IBFD of (18) is severely limited by the SI. We will demonstrate in our simulation results of Sec. IV that the IBFD can only achieve a higher bandwidth efficiency, when a sufficiently high signal transmission power is provided.

III. PROPOSED BEAMFORMING AIDED MDD FOR mm-WAVE COMMUNICATIONS

In this section, we briefly address the dynamic range of the PA at the transmitter and of the ADC at the receiver. Then our beamforming aided SI cancellation scheme is presented.

A. DYNAMIC RANGE OF PA

It is widely known that as a result of the IDFT operation, the PAPR of the OFDM signals grows linearly with the number of subcarriers. To elaborate, the dynamic range of the PA at the transmitter is dependent on the PAPR, which is portrayed in Fig. 4. In the classic PA design, the Input Back-Off (IBO) is defined by the ratio of maximum voltage supply and average input power [45]–[47]. For the signals associated

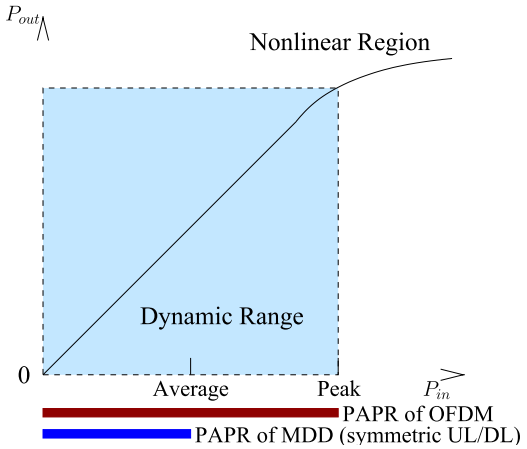

FIGURE 4. The dynamic range of the Power Amplifier (PA) at the transmitter (Tx).

with a high PAPR, a large IBO is required in order to avoid the saturation of signals in the non-linear range of the transfer characteristic seen in Fig. 4. By contrast, having a high IBO degrades the PA efficiency.

The trend of modern circuitry design indicates that the IBO provided by the commercially available PAs generally decreases as the carrier frequency increases [48]. In the most up-to-date 5G standards [18], only the lower frequency range of the Ka-band (27 GHz–40 GHz) is utilized from the wider mmWave spectrum (30 GHz–300 GHz). In fact, processing the OFDM signals associated with high PAPR becomes increasingly challenging in the higher frequency range of the mmWave band that approaches the edge of the Terahertz band (0.1 THz–10 THz), which is envisioned to be a potential key enabler of the future 6G [48]–[52].

More explicitly, let us firstly consider the L-ary PSK constellation of $\{s^l = \exp(j\frac{2\pi}{L}l)\}_{l=0}^{L}$. The peak power of the time-domain OFDM sample of $x(n) = \frac{1}{\sqrt{N}}\sum_{\kappa=0}^{N-1} s(\kappa)w_N^{\kappa n}$ is reached, when modulating all subcarriers by $\{s(\kappa) = 1\}_{\kappa=0}^{N-1}$ at $n = 0$, which results in PAPR $= N$ [53]. Moreover, let us consider employing L-ary QAM having symbols of the form $\{\{s^{\iota_I,\iota_Q} = \frac{\sqrt{L}-2\iota_I-1}{\sqrt{\beta}} + j\frac{\sqrt{L}-2\iota_Q-1}{\sqrt{\beta}}\}_{\iota_I=0}^{\sqrt{L}-1}\}_{\iota_Q=0}^{\sqrt{L}-1}$ for the frequency-domain OFDM symbol $\{s(\kappa)\}_{\kappa=0}^{N-1}$, where the normalization factor is $\beta = \frac{\sum_{\iota_I=0}^{\sqrt{L}/2-1}\sum_{\iota_Q=0}^{\sqrt{L}/2-1}[(\sqrt{L}-2\iota_I-1)^2+(\sqrt{L}-2\iota_Q-1)^2]}{L/4} = \frac{2(L-1)}{3}$ [54], [55]. The peak power of the time-domain OFDM sample of $x(n) = \frac{1}{\sqrt{N}}\sum_{\kappa=0}^{N-1} s(\kappa)w_N^{\kappa n}$ is obtained, when modulating all subcarriers by the maximum-power QAM symbol of $\{s(\kappa) = \frac{\sqrt{L}-1}{\sqrt{\beta}} + j\frac{\sqrt{L}-1}{\sqrt{\beta}}\}_{\kappa=0}^{N-1}$ at $n = 0$, which results in $x(0) = \frac{1}{\sqrt{N}}\sum_{\kappa=0}^{N-1}\left(\frac{\sqrt{L}-1}{\sqrt{\beta}} + j\frac{\sqrt{L}-1}{\sqrt{\beta}}\right) = \sqrt{N}\left(\frac{\sqrt{L}-1}{\sqrt{\beta}} + j\frac{\sqrt{L}-1}{\sqrt{\beta}}\right)$. The average OFDM sample power remains unity. In summary, the resultant OFDM PAPR is given by [54], [56]:

$$\text{PAPR} = \frac{2N(\sqrt{L}-1)^2}{\beta} = \frac{3N(\sqrt{L}-1)}{\sqrt{L}+1}. \tag{19}$$

Although the probability of occurrence of the signals having the peak-power decreases with both N and L, the OFDM systems typically still have to invoke PAPR reduction techniques including active constellation extension, selected mapping, tone injection and tone reservation [20]–[23]. In recent years, Subcarrier Index Modulation (SIM) [54], [57]–[59] has attracted substantial attention, which activates a subset of subcarriers, where the activation indices implicitly carry extra source information. The resultant PAPR reduction constitutes one of the key benefits of the SIM design [54], [57]–[59]. The MDD is similar to the SIM in the way that only a subset of subcarriers are activated for each link, which effectively reduces the PAPR without involving extra signal processing complexity and analog circuitry. Fig. 5 confirms that in the case of symmetric traffic, the MDD exhibits a substantially reduced PAPR compared to the HD and IBFD modes.

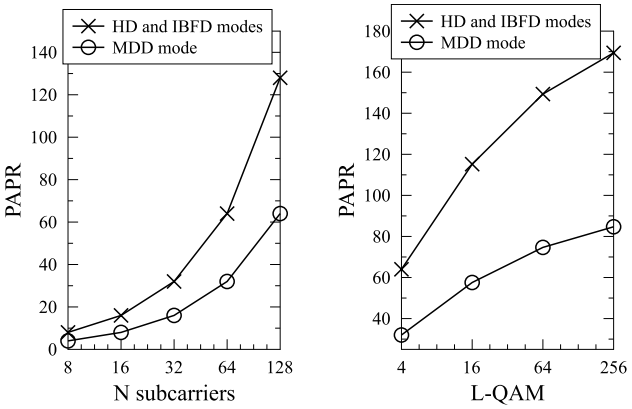

(a) N={8,16,32,64,128}, QPSK (b) N=64, {4,16,64,256}QAM

FIGURE 5. PAPR Comparison between the OFDM aided HD, IBFD as well as MDD.

In realistic cellular networks, however, typically asymmetric traffic is encountered, where the UL-to-DL traffic ratio is commonly reported to be 2:8 or even 1:9 [60]. Therefore, the MDD is even more favorable in terms of energy-efficiency in these scenarios, where the UL only has to activate a small portion of the OFDM subcarriers. This results in substantially reduced power consumption for the MSs having a compact form-factor MSs. Nonetheless, without diverting from the specific focus of this work, we set aside the MDD study of asymmetric traffic for our future work.

B. DYNAMIC RANGE OF ADC

In order to address the dynamic range of the ADC in the presence of strong SI in the FD modes, let us consider the transmit power of $P_{Tx} = 22$ dBm as well as the ULA parameters of $d = 10\lambda$ and $\vartheta = 160°$ at both the nodes. The carrier frequency is $f = 30$ GHz. The two nodes are separated by $d_{P2P} = 5$m. The beamforming gain is assumed to be $G_{BF} = 20$ dB. As a result, first of all, the received SI power is given by $P_{Rx}^{SI} = P_{Tx} - G_{FSPL}^{SI} + G_{BF} = 22$ dBm $- 20\log_{10}(40\pi)$ dB $+ 20$ dB $= 0$ dBm, where the Free-Space Path Loss (FSPL) is evaluated by $G_{FSPL}^{SI} = 20\log_{10}(\frac{4\pi d}{\lambda})$ dB.

Similarly, the received power of the desired signal is given by $P_{Rx}^{ij} = P_{Tx} - G_{FSPL}^{ij} + G_{BF} = 22\,\text{dBm} - 20\log_{10}(\frac{4\pi d_{P2P}}{\lambda})\,\text{dB} + 20\,\text{dB} = -34\,\text{dBm}$. As a result, the SI is $P_{Rx}^{SI} - P_{Rx}^{ij} = 34$ dB higher than the desired signal, which is more than 2000 time different in power strength. Therefore, the rule-of-thumb ADC dynamic range of $6.02Q$ dB is deemed to be completely dominated by the SI, where Q refers to the ADC resolution bits, as portrayed by Fig. 6. As a result, the SI-to-Quantization Noise power Ratio (SIQNR) may be approximately represented by $SIQNR = 6.02Q = 48.2$ dB, assuming a $Q = 8$ bits ADC resolution.

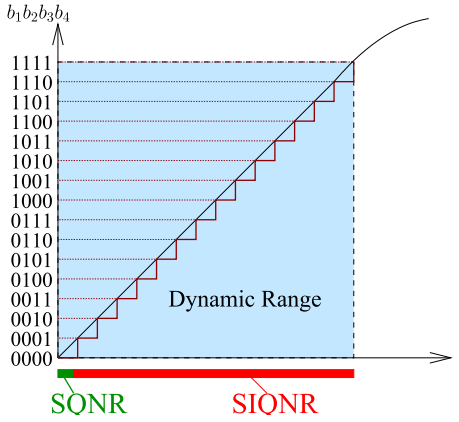

FIGURE 6. The dynamic range of the Analog-to-Digital Converter (ADC) at the receiver (Rx).

Secondly, let us proceed to evaluate the ADC quantization noise power according to $P_{QN} = P_{Rx}^{SI} - 6.02Q = -48.2$ dBm. As a result, the effective ADC dynamic range for the desired signal is defined by the Signal-to-Quantization Noise power Ratio (SQNR) as $SQNR = P_{Rx}^{ij} - P_{QN} = 14.2$ dB, which corresponds to a substantially reduced $\overline{Q} = SQNR/6.02 = 2.4$ effective ADC bitwidth, compared to the $Q = 8$-bit ADC resolution provided.

Fig. 7 portrays the ADC dynamic ranges according to the above evaluations, where the effective SQNR is shown to be substantially lower than the SIQNR. More explicitly, Fig. 7(a) evidences that when provided with $Q < 7$ bits, the effective ADC bitwidth available for the desired signal falls even below 1 bit. Moreover, Fig. 7(b) further demonstrates that when the separation distance grows beyond $d_{P2P} > 11$m, the effective SQNR once again falls below 1 bit. Therefore, it is of crucial importance to mitigate the SI before the signal enters the ADC, so that the signal detection of the FD mode satisfies the realistic requirements.

C. BEAMFORMING WITH NULL-SPACE PROJECTION

In the inherent beamforming structure of mmWave communication, the LoS SI can be completely eliminated by creating a null in the SI direction, as portrayed in Fig. 8. This problem can be formulated by adding a null-space projection constraint to the beamforming gain maximization problem as follows:

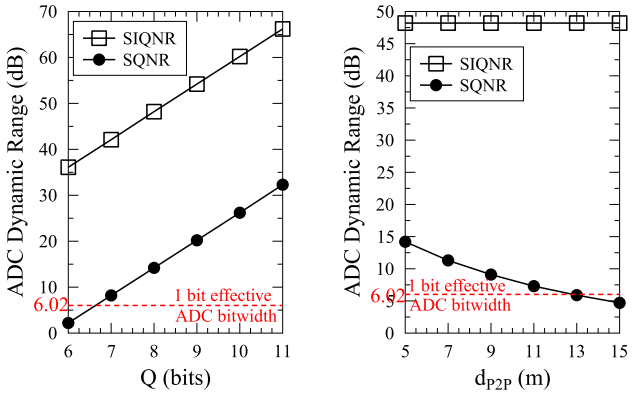

FIGURE 7. Comparison between the ADC dynamic range that is dominated by the SI-to-Quantization Noise power Ratio (SIQNR) and the effective ADC dynamic range of the desired Signal-to-Quantization Noise power Ratio (SQNR).

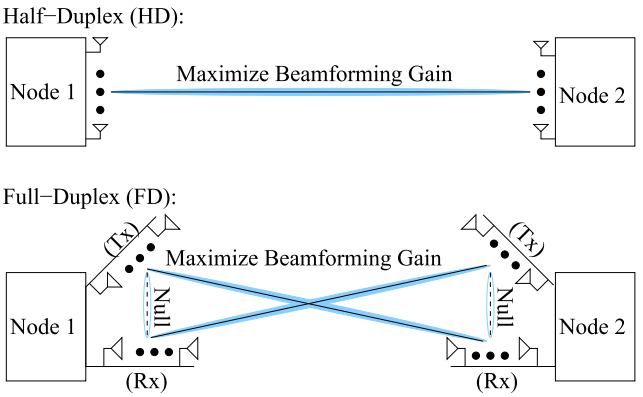

FIGURE 8. Schematic descriptions of beamforming aided Half-Duplex (HD) and Full-Duplex (FD) schemes, where the null-space cancelling is imposed for the Self-Interference (SI) in FD.

Problem 1: Maximize the beamforming gains over all the multipath components, while nulling the strongest component of SI, i.e.

$$\max_{\mathbf{w}_{r1},\mathbf{w}_{t1},\mathbf{w}_{r2},\mathbf{w}_{t2}} \Psi = \sum_{l=0}^{N_c-1} |\mathbf{w}_{r1}^H \mathbf{H}_l^{12} \mathbf{w}_{t2}|^2 + |\mathbf{w}_{r2}^H \mathbf{H}_l^{21} \mathbf{w}_{t1}|^2,$$
$$\text{s.t. } \mathbf{w}_{r1}^H \mathbf{H}_0^{11} \mathbf{w}_{t1} = \mathbf{w}_{r2}^H \mathbf{H}_0^{22} \mathbf{w}_{t2} = 0, \tag{20}$$

where $\{\mathbf{w}_{ri}\}_{i=1}^2$ and $\{\mathbf{w}_{ti}\}_{i=1}^2$ are unit-norm vectors.

The problem in (20) is non-convex. What is even worse is that the optimization variables associated with both the nodes are inseparable. Hence we simplify this problem as follows.

Problem 2: Maximize the beamforming gain over each node separately, while nulling the strongest SI component, i.e.

$$\max_{\mathbf{w}_{ri},\mathbf{w}_{tj}} \sum_{l=0}^{N_c-1} |\mathbf{w}_{ri}^H \mathbf{H}_l^{ij} \mathbf{w}_{tj}|^2, \quad \text{s.t. } \mathbf{H}_0^{ij} \mathbf{w}_{tj} = \mathbf{0}, \tag{21}$$

where $(i, j) \in \{(1, 2), (2, 1)\}$. To elaborate, the constraint in (21) may be satisfied by the right null-space projection as follows:

Proposition 1: In order to arrive at $\mathbf{H}_0^{ij}\mathbf{w}_{tj} = \mathbf{0}$, the transmit beamforming vector is generated by:

$$\mathbf{w}_{tj} = \mathbf{P}_{\mathcal{N}_R}(\mathbf{H}_0^{ij})\overline{\mathbf{w}}_{tj}, \tag{22}$$

where $\mathbf{P}_{\mathcal{N}_R}(\cdot) \in \mathbb{C}^{N_{tj}\times N_{tj}}$ is the right null-space projection matrix, while $\overline{\mathbf{w}}_{tj} \in \mathbb{C}^{N_{tj}\times 1}$ is an arbitrary vector that is chosen for maximizing the beamforming gain of (21). Moreover, $\{N_{tj} > N_{rj}\}_{j=1}^{2}$ is required.

Proof: According to (22), we have:

$$\mathbf{P}_{\mathcal{N}_R}(\mathbf{H}_0^{ij}) = \mathbf{I}_{N_{tj}} - (\mathbf{H}_0^{ij})^H \left[\mathbf{H}_0^{ij}(\mathbf{H}_0^{ij})^H\right]^{-1}\mathbf{H}_0^{ij}. \tag{23}$$

As a result, the constraint $\mathbf{H}_0^{ij}\mathbf{w}_{tj} = \mathbf{H}_0^{ij}\mathbf{P}_{\mathcal{N}_R}(\mathbf{H}_0^{ij})\overline{\mathbf{w}}_{tj} = \mathbf{0}$ is guaranteed, regardless of the values in $\overline{\mathbf{w}}_{tj}$, provided that the right null-space of $\mathbf{H}_0^{ij}$ is non-empty, i.e. we have[2] $\mathcal{N}_R(\mathbf{H}_0^{ij}) \neq \phi$, which translates to $N_{tj} > N_{rj}$. □

Therefore, the problem in (21) may now be reformulated as follows:

Problem 3: Maximize the beamforming gain over each node separately, while ensuring that $\mathbf{w}_{tj} = \mathbf{P}_{\mathcal{N}_R}(\mathbf{H}_0^{ij})\overline{\mathbf{w}}_{tj}$, i.e.

$$\max_{\mathbf{w}_{ri},\overline{\mathbf{w}}_{tj}} \sum_{l=0}^{N_c-1} |\mathbf{w}_{ri}^H\mathbf{H}_l^{ij}\mathbf{P}_{\mathcal{N}_R}(\mathbf{H}_0^{ij})\overline{\mathbf{w}}_{tj}|^2. \tag{24}$$

Although the optimization problem in (24) is non-convex, a local optimum can be found by employing an algorithm analogous to the Iterative Eigenvalue Decomposition (IEVD) [38]. The proposed Projection aided IEVD (P-IEVD) is presented in Algorithm 1. Note that IEVD [38] can be viewed as a special case of the proposed P-IEVD, and P-IEVD reduces to IEVD when the projection matrix becomes an identity matrix as $\mathbf{P}_{\mathcal{N}_R}(\mathbf{H}_0^{ij}) = \mathbf{I}_{N_{tj}}$.

Note that a few iterations are sufficient for the convergence of Algorithm 1, as it will be shown in the next section. Furthermore, the P-IEVD requires full CSI for obtaining the optimal transmit and receive beamforming vectors. Acquiring full CSI would impose significant overhead owing to the large number of channel coefficients to be estimated. We adopt a training based approach for implementing our P-IEVD, which is described in Algorithm 2. The proposed training based P-IEVD amalgamates the channel estimation and the beamforming vector design procedures, which avoids the overhead involved in acquiring the CSI explicitly. Specifically, the proposed training based P-IEVD exploits the channel's reciprocity and the low-complexity *power method*[3] of [61] for computing the principal Eigenvector. Furthermore, the convergence behavior of Algorithm 2 is the same as that of Algorithm 1, as it will be shown in the next section.

Algorithm 1 The P-IEVD Scheme

Require: Randomly chosen unit-norm receive beamforming vector $\mathbf{w}_{ri}$ and max_iterations.

while $k <$ max_iterations **do**

1. Compute the Eigenvalue decomposition of $\mathbf{P}_{\mathcal{N}_R}(\mathbf{H}_0^{ij})\left(\sum_{l=0}^{N_c-1}\mathbf{H}_l^{ij^H}\mathbf{w}_{ri}\mathbf{w}_{ri}^H\mathbf{H}_l^{ij}\right)\mathbf{P}_{\mathcal{N}_R}(\mathbf{H}_0^{ij})$ and set the principal Eigenvector to $\overline{\mathbf{w}}_{tj}$.
2. Compute the Eigenvalue decomposition of $\sum_{l=0}^{N_c-1}\mathbf{H}_l^{ij}\mathbf{P}_{\mathcal{N}_R}(\mathbf{H}_0^{ij})\overline{\mathbf{w}}_{tj}\overline{\mathbf{w}}_{tj}^H\mathbf{P}_{\mathcal{N}_R}(\mathbf{H}_0^{ij})\mathbf{H}_l^{ij^H}$ and set the principal Eigenvector to $\mathbf{w}_{ri}$.
3. $k := k + 1$.

end while

Algorithm 2 The Training Based P-IEVD Scheme

Require: Randomly chosen unit-norm receive beamforming vector $\mathbf{w}_{ri}$ and max_iterations.

while $k <$ max_iterations **do**

1. Obtain $\{\mathbf{z}_l(t) = \mathbf{e}_t^H\mathbf{H}_l^{ij^H}\mathbf{w}_{ri}\}_{t=1}^{N_{tj}}$ for $l = \{0, 1, \ldots, N_c - 1\}$ by using training sequences $\{\mathbf{e}_t\}_{t=1}^{N_{tj}}$ for N_{tj} slots, where $\mathbf{e}_t \in \mathbb{C}^{N_{tj}\times 1}$ denotes the t-th column of the identity matrix $\mathbf{I}_{N_{tj}}$. Then we arrive at the noise-contaminated estimation of $\mathbf{z}_l = \mathbf{H}_l^{ij^H}\mathbf{w}_{ri}$.
2. Compute $\mathbf{R}^{ij} = \sum_{l=0}^{N_c-1}\mathbf{z}_l\mathbf{z}_l^H$, $\mathbf{R}_{eff}^{ij} = \mathbf{P}_{\mathcal{N}_R}(\mathbf{H}_0^{ij})\mathbf{R}^{ij}\mathbf{P}_{\mathcal{N}_R}(\mathbf{H}_0^{ij})$, and $\overline{\mathbf{w}}_{tj} = \mathbf{R}_{eff}^{ij^K}\mathbf{e}_1/\|\mathbf{R}_{eff}^{ij^K}\mathbf{e}_1\|$.
3. Obtain $\{\bar{\mathbf{z}}_l(\tau) = \bar{\mathbf{e}}_\tau^H\mathbf{H}_l^{ij}\overline{\mathbf{w}}_{tj}\}_{\tau=1}^{N_{ri}}$ for $l = \{0, 1, \ldots, N_c - 1\}$ by using training sequences $\{\bar{\mathbf{e}}_\tau\}_{\tau=1}^{N_{ri}}$ for N_{ri} slots, where $\bar{\mathbf{e}}_\tau \in \mathbb{C}^{N_{ri}\times 1}$ denotes the τ-th column of the identity matrix $\mathbf{I}_{N_{ri}}$. Then we arrive at the noise-contaminated estimation of $\bar{\mathbf{z}}_l = \mathbf{H}_l^{ij}\overline{\mathbf{w}}_{tj}$.
4. Compute $\bar{\mathbf{R}}^{ij} = \sum_{l=0}^{N_c-1}\bar{\mathbf{z}}_l\bar{\mathbf{z}}_l^H$ and $\mathbf{w}_{ri} = \bar{\mathbf{R}}^{ij^K}\bar{\mathbf{e}}_1/\|\bar{\mathbf{R}}^{ij^K}\bar{\mathbf{e}}_1\|$.
5. $k := k + 1$.

end while

D. ALTERNATIVE SI CANCELLATION ARCHITECTURES

The feasibility condition of $\{N_{tj} > N_{rj}\}_{j=1}^{2}$ is imposed in Problem 2. In order to adapt to different MIMO setups, we briefly discuss alternative architectures in this section.

First of all, in contrast to (21), the problem in (20) can be simplified as follows:

Problem 4: Maximize the beamforming gain over each node separately, while nulling the strongest component of SI, i.e.

$$\max_{\mathbf{w}_{ri},\mathbf{w}_{tj}} \sum_{l=0}^{N_c-1} |\mathbf{w}_{ri}^H\mathbf{H}_l^{ij}\mathbf{w}_{tj}|^2, \quad \text{s.t. } \mathbf{w}_{ri}^H\mathbf{H}_0^{ii} = \mathbf{0}, \tag{25}$$

where $(i, j) \in \{(1, 2), (2, 1)\}$. In order to arrive at a non-trivial $\mathbf{w}_{ri}$, the feasibility condition in (25) requires that the left null-space of $\mathbf{H}_0^{ii}$ be non-empty. Thus, we need[4] $\{\mathcal{N}_L(\mathbf{H}_0^{ii}) \neq \phi\}_{i=1}^{2}$, which translates to $\{N_{ti} < N_{ri}\}_{i=1}^{2}$. Assuming that the feasibility conditions are satisfied, the problem in (25) can be equivalently written as follows:

[2] $\mathcal{N}_R(\mathbf{A})$ represents the right null-space of $\mathbf{A}$.

[3] Given an $m \times m$ matrix $\mathbf{A}$, its principal Eigenvector can be obtained by computing $\mathbf{A}^K\mathbf{e}_1/\|\mathbf{A}^K\mathbf{e}_1\|$ for sufficiently large K, where $\mathbf{e}_1$ is the first column of $m \times m$ identity matrix.

[4] $\mathcal{N}_L(\mathbf{A})$ represents the left null-space of $\mathbf{A}$.

TABLE 3. Summary of the optimization problems and the feasibility conditions associated with various SI cancellation architectures.

Optimization problem	Feasibility condition
$\max_{\mathbf{w}_{ri},\overline{\mathbf{w}}_{tj}} \sum_{l=0}^{N_c-1} \lvert\mathbf{w}_{ri}^H\mathbf{H}_l^{ij}\mathbf{P}_{\mathcal{N}_R}(\mathbf{H}_0^{jj})\overline{\mathbf{w}}_{tj}\rvert^2$.	$\mathbf{w}_{tj} = \mathbf{P}_{\mathcal{N}_R}(\mathbf{H}_0^{jj})\overline{\mathbf{w}}_{tj}$, $N_{t1} > N_{r1}$, $N_{t2} > N_{r2}$.
$\max_{\overline{\mathbf{w}}_{ri},\mathbf{w}_{tj}} \sum_{l=0}^{N_c-1} \lvert\overline{\mathbf{w}}_{ri}^H\mathbf{P}_{\mathcal{N}_L}(\mathbf{H}_0^{ii})\mathbf{H}_l^{ij}\mathbf{w}_{tj}\rvert^2$.	$\mathbf{w}_{ri}^H = \overline{\mathbf{w}}_{ri}^H\mathbf{P}_{\mathcal{N}_L}(\mathbf{H}_0^{ii})$, $N_{t1} < N_{r1}$, $N_{t2} < N_{r2}$.
$\max_{\mathbf{w}_{r1},\mathbf{w}_{t2}} \sum_{l=0}^{N_c-1} \lvert\mathbf{w}_{r1}^H\mathbf{H}_l^{12}\mathbf{w}_{t2}\rvert^2$ $\max_{\overline{\mathbf{w}}_{r2},\overline{\mathbf{w}}_{t1}} \sum_{l=0}^{N_c-1} \lvert\overline{\mathbf{w}}_{r2}^H\mathbf{P}_{\mathcal{N}_L}(\mathbf{H}_0^{22})\mathbf{H}_l^{21}\mathbf{P}_{\mathcal{N}_R}(\mathbf{H}_0^{11})\overline{\mathbf{w}}_{t1}\rvert^2$.	$\mathbf{w}_{r2}^H = \overline{\mathbf{w}}_{r2}^H\mathbf{P}_{\mathcal{N}_L}(\mathbf{H}_0^{22})$, $\mathbf{w}_{t1} = \mathbf{P}_{\mathcal{N}_R}(\mathbf{H}_0^{11})\overline{\mathbf{w}}_{t1}$, $N_{t1} > N_{r1}$, $N_{t2} < N_{r2}$.

Problem 5: Maximize the beamforming gain over each node separately, while ensuring that $\mathbf{w}_{ri}^H = \overline{\mathbf{w}}_{ri}^H\mathbf{P}_{\mathcal{N}_L}(\mathbf{H}_0^{ii})$, i.e.

$$\max_{\overline{\mathbf{w}}_{ri},\mathbf{w}_{tj}} \sum_{l=0}^{N_c-1} |\overline{\mathbf{w}}_{ri}^H\mathbf{P}_{\mathcal{N}_L}(\mathbf{H}_0^{ii})\mathbf{H}_l^{ij}\mathbf{w}_{tj}|^2, \tag{26}$$

where the projection matrix that projects on to the left null-space of $\mathbf{H}_0^{ii}$ is given by:

$$\mathbf{P}_{\mathcal{N}_L}(\mathbf{H}_0^{ii}) = \mathbf{I}_{N_{ri}} - \mathbf{H}_0^{ii}\left[(\mathbf{H}_0^{ii})^H\mathbf{H}_0^{ii}\right]^{-1}(\mathbf{H}_0^{ii})^H. \tag{27}$$

Alternatively, the problem in (20) can also be simplified as follows:

Problem 6: Maximize the beamforming gain over each node separately, while nulling the strongest component of SI, i.e.

$$\begin{aligned}&\max_{\mathbf{w}_{r1},\mathbf{w}_{t2}} \sum_{l=0}^{N_c-1} |\mathbf{w}_{r1}^H\mathbf{H}_l^{12}\mathbf{w}_{t2}|^2,\\ &\max_{\mathbf{w}_{r2},\mathbf{w}_{t1}} \sum_{l=0}^{N_c-1} |\mathbf{w}_{r2}^H\mathbf{H}_l^{21}\mathbf{w}_{t1}|^2,\\ &\text{s.t. } \mathbf{w}_{r2}^H\mathbf{H}_0^{22} = \mathbf{0} \text{ and } \mathbf{H}_0^{11}\mathbf{w}_{t1} = \mathbf{0}.\end{aligned} \tag{28}$$

In order to arrive at non-trivial $\mathbf{w}_{r2}$ and $\mathbf{w}_{t1}$, the feasibility condition in (28) requires that the left null-space of $\mathbf{H}_0^{22}$ and the right null-space of $\mathbf{H}_0^{11}$ be non-empty. Thus, we require $\mathcal{N}_L(\mathbf{H}_0^{22}) \neq \phi$ and $\mathcal{N}_R(\mathbf{H}_0^{11}) \neq \phi$, which translates to $N_{t1} > N_{r1}$ and $N_{t2} < N_{r2}$. As a result, the problem in (28) can be equivalently written as follows.

Problem 7: Maximize the beamforming gain over each node separately, while ensuring that $\mathbf{w}_{r2}^H = \overline{\mathbf{w}}_{r2}^H\mathbf{P}_{\mathcal{N}_L}(\mathbf{H}_0^{22})$ and $\mathbf{w}_{t1} = \mathbf{P}_{\mathcal{N}_R}(\mathbf{H}_0^{11})\overline{\mathbf{w}}_{t1}$, i.e.

$$\max_{\mathbf{w}_{r1},\mathbf{w}_{t2}} \sum_{l=0}^{N_c-1} |\mathbf{w}_{r1}^H\mathbf{H}_l^{12}\mathbf{w}_{t2}|^2, \tag{29}$$

$$\max_{\overline{\mathbf{w}}_{r2},\overline{\mathbf{w}}_{t1}} \sum_{l=0}^{N_c-1} |\overline{\mathbf{w}}_{r2}^H\mathbf{P}_{\mathcal{N}_L}(\mathbf{H}_0^{22})\mathbf{H}_l^{21}\mathbf{P}_{\mathcal{N}_R}(\mathbf{H}_0^{11})\overline{\mathbf{w}}_{t1}|^2. \tag{30}$$

It is readilty seen that the optimization problems in Problem 5 and Problem 7 can be similarly solved by employing the P-IEVD algorithm. Table 3 summarizes the optimization problems and the feasibility conditions associated with the various SI cancellation architectures.

IV. SIMULATION STUDIES

Simulation scenario: In all our simulations, both the nodes are assumed to have $d = 10\lambda$ and $\vartheta = 160°$. The frequency-selective mmWave channel is assumed to have $D = 8$, $N_c = 5$, $N_{ray} = 8$ and $\sigma_\theta = \sigma_\phi = 5°$. The number of subcarriers in each OFDM symbol is assumed to be 64. The parameters are summarized in Table 4.

TABLE 4. Simulation parameters.

Carrier frequency	30 GHz
OFDM subcarriers	64
ULA geometry	$d = 10\lambda$ and $\vartheta = 160^o$
Channel model	Frequency-selective mmWave channels
MPC delay distribution	Uniform over $[0, 1, \cdots, D]$
MPC maximum delay	$D = 8$
MPC clusters	$N_c = 5$
MPCs per cluster	$N_{ray} = 8$
MPC distribution	$\mathcal{CN}(0, 1)$ with AoA and AoD
AoA/AoD distribution	Laplacian
AoA/AoD means	Uniform over $[0, 2\pi)$
AoA/AoD variances	$\sigma_\theta = \sigma_\phi = 5^o$

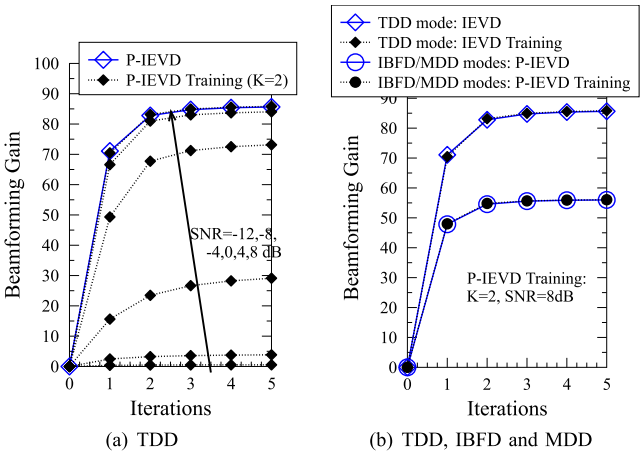

(a) TDD (b) TDD, IBFD and MDD

FIGURE 9. Variation in the beamforming gains as a function of iterations in TDD, IBFD and MDD systems having $N_{t1} = N_{t2} = 8$, $N_{r1} = N_{r2} = 4$ and $\rho_{ii} = 15$ dB.

The beamforming gains achieved by the proposed P-IEVD are portrayed by Fig. 9. We note that as discussed in Sec. III.C, the proposed P-IEVD subsumes the IEVD of [38] as a special case, where the projection matrix for the TDD mode is simply the identity matrix. Fig. 9 demonstrates that $K = 2$ iterations are sufficient for the convergence of the proposed P-IEVD algorithms, and the performance of the training based algorithm improves as the SNR increases. Furthermore, it is evidenced by Fig. 9(b) that the beamforming gain of the TDD mode is higher than that of the FD modes of IBFD/MDD, owing to the fact that the HD TDD mode does not need to perform null-space LoS SI cancellation, as depicted earlier in Fig. 8. On one hand, the TDD mode indeed benefits from a higher degree-of-freedom on beamforming gain. On the other hand, compared to the FD

modes of IBFD/MDD, the TDD mode is a HD scheme that requires guard interval, which degrades its overall bandwidth efficiency after normalization. This issue will be addressed later in this section.

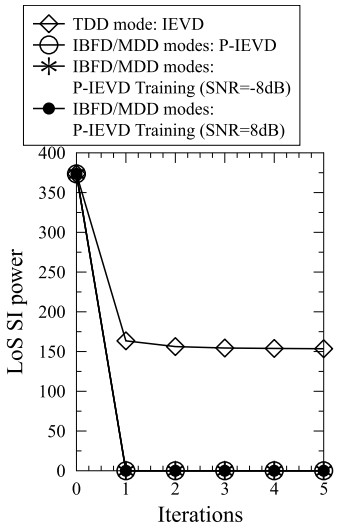

FIGURE 10. The LoS SI power as a function of iterations in TDD, IBFD and MDD systems having $N_{t1} = N_{t2} = 8$, $N_{r1} = N_{r2} = 4$ and $\rho_{ii} = 15$ dB.

The LoS SI power $\|\mathbf{w}_{ri}^H \mathbf{H}_0^{ii} \mathbf{w}_{ti}\|^2$ seen in (1) is examined for the proposed P-IEVD in Fig. 10. First of all, the IEVD aided TDD scheme of [38] does not deal with the SI. Therefore, during the signal transmission of one link, the signal reception for the other link has to be postponed in order to avoid encountering a high SI power, as seen in Fig. 10. Secondly, Fig. 10 confirms that after $K = 1$ iteration, the proposed P-IEVD aided IBFD/MDD arrangements successfully adjust the beamforming weights for completely eliminating the LoS SI power, where the training at different SNRs does not affect the SI mitigation. We note that upon ensuring $\|\mathbf{w}_{ri}^H \mathbf{H}_0^{ii} \mathbf{w}_{ti}\|^2 = 0$, the LoS SI term is completely eliminated from the received signal in (1), which is delivered to the ADC without any contamination by the strong LoS SI power. Nonetheless, we will proceed to demonstrate that the NLoS SI seen in (1) may still degrade the performance of IBFD, which is avoided by the MDD design, thanks to its beneficial orthogonal subcarrier division duplexing.

Fig. 11 demonstrates that the training based P-IEVD scheme of Algorithm 2 exhibits a bandwidth efficiency degradation in the low-SNR region, owing to the fact that the CSI estimation required by beamforming is contaminated by noise. Nonetheless, it is confirmed by Fig. 11 that the training based P-IEVD algorithms perform close to their ideal P-IEVD counterparts of Algorithm 1, as the SNR increases. Without loss of generality, the P-IEVD scheme associated with $K = 2$ iterations is invoked for our bandwidth efficiency comparisons in the rest of this section. Moreover, without ambiguity, the terminology of "bandwidth efficiency" is quantified for each node, as presented in Sec. II, while "average bandwidth efficiency" refers to the overall metric that is normalized by the number of nodes.

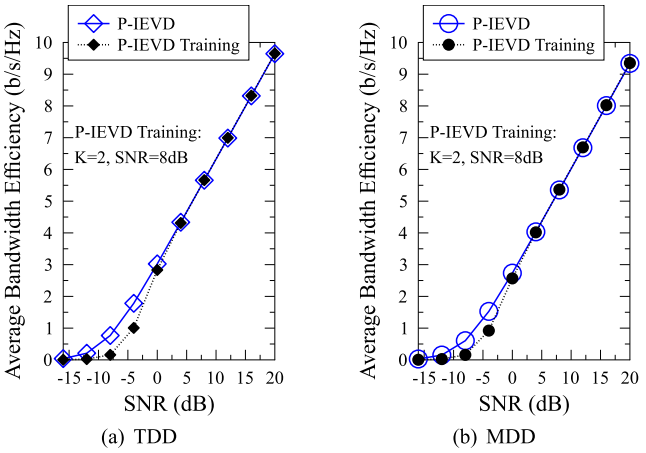

FIGURE 11. Average bandwidth efficiency in TDD and MDD systems having $N_{t1} = N_{t2} = 8$, $N_{r1} = N_{r2} = 4$ and $\rho_{ii} = 15$ dB.

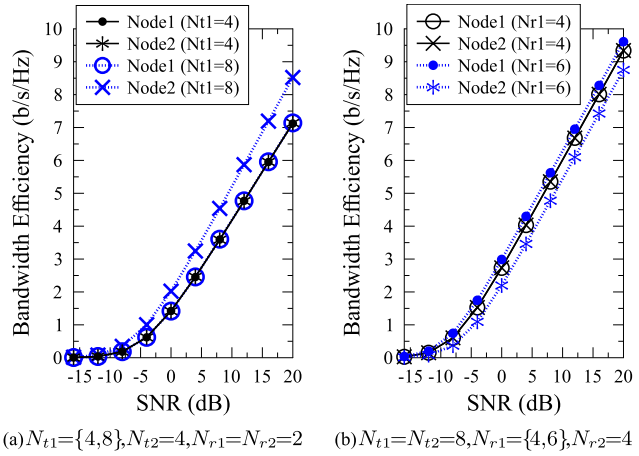

FIGURE 12. Bandwidth efficiency in MDD systems having symmetric and asymmetric MIMO setups.

Fig. 12 studies the effect of both symmetric and asymmetric MIMO setups. It can be seen in Fig. 12 that the symmetric traffic is recorded for the symmetric MIMO setup of $N_{t1} = N_{t2}$ and $N_{r1} = N_{r2}$. Furthermore, when a higher number of TAs is employed at Node 1 as $N_{t1} > N_{t2}$, the bandwidth efficiency is improved at Node 2, as shown in Fig. 12(a), owing to the improved beamforming gain. Moreover, Fig. 12(b) demonstrates that increasing the number of RAs at Node 1 as $N_{r1} > N_{r2}$ results in an improved performance recorded at Node 1.

Finally, our performance comparison between TDD, IBFD and MDD is offered in Fig. 13. The guard interval of the TDD mode is configured to 1/14 for LTE-A and 12.5% for IEEE 802.11ad. We note that in a variety of systems, the guard interval may be further increased in order to increase the coverage area. For example, the guard interval for IEEE 802.11ac and DVB-T may be as high as 20% and 25%, respectively, which are not included in Fig. 13(b) to avoid obfuscation.

TABLE 5. Summary of bandwidth efficiency gains of MDD (dynamic allocation) over TDD (IEEE 802.11ad) and OBFD based on Fig. 13(b).

	SNR=0 dB	SNR=4 dB	SNR=8 dB	SNR=12 dB	SNR=16 dB	SNR=20 dB	SNR=24 dB	SNR=28 dB
MDD over TDD	0.46 b/s/Hz	0.62 b/s/Hz	0.8 b/s/Hz	0.98 b/s/Hz	1.14 b/s/Hz	1.32 b/s/Hz	1.47 b/s/Hz	1.66 b/s/Hz
MDD over IBFD	3.02 b/s/Hz	4.1 b/s/Hz	4.83 b/s/Hz	4.9 b/s/Hz	4.25 b/s/Hz	3.16 b/s/Hz	1.88 b/s/Hz	0.6 b/s/Hz

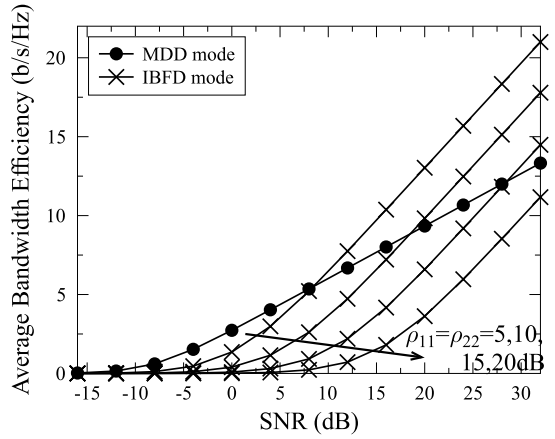

(a) $\rho_{ii} = \{5, 10, 15, 20\}$dB

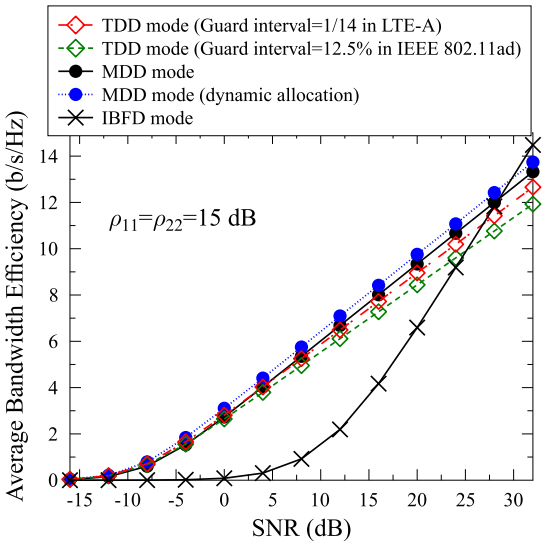

(b) $\rho_{ii} = 15$dB

FIGURE 13. Average bandwidth efficiency in TDD, IBFD and MDD modes in a system having $N_{t1} = N_{t2} = 8$, $N_{r1} = N_{r2} = 4$ and $\rho_{ii} = \{5, 10, 15, 20\}$ dB. The guard interval for the TDD is configured to {1/14, 12.5%} for LTE-A and IEEE 802.11ad.

It is evidenced by Fig. 13(a) that the performance of IBFD degrades as the power of NLoS SI of (1) increases. To elaborate, our proposed P-IEVD algorithm only eliminates the LoS SI of (1). As a result, the residual NLoS SI imposes an increased noise power on the IBFD signal detection in (18). By contrast, the MDD assigns separate OFDM subcarriers to different links. Therefore, the MDD signal detection in (16) is "clean" and free from SI.

Fig. 13(b) demonstrates that first of all, the dynamic subcarrier allocation of (14) improves the MDD performance. Secondly, owing to the guard interval, the TDD mode becomes inferior to the MDD mode after normalization, despite the fact that the TDD mode achieves a higher beamforming gain. Thirdly, although the IBFD endeavors to exploit the frequency-time resources to the fullest possible extent, its SI-contaminated performance is only advantageous, when a sufficiently high SNR $>$ 30 dB is provided.

V. CONCLUSION

We have proposed a FD scheme for frequency-selective mmWave channels. In order to mitigate the detrimental effects of SI imposed on the ADC dynamic range, the novel P-IEVD and its training based counterpart were proposed, where the nullspace SI cancellation is intrinsically amalgamated with the beamforming structure of mmWave communication. Our simulation results demonstrate that in addition to the substantially reduced PAPR of signal transmission, the MDD mode is capable of outperforming both of its HD TDD and IBFD counterparts in dispersive mmWave channels, as summarized in Table 5 based on Fig. 13(b).

REFERENCES

[1] Z. Zhang, K. Long, A. V. Vasilakos, and L. Hanzo, "Full-duplex wireless communications: Challenges, solutions, and future research directions," *Proc. IEEE*, vol. 104, no. 7, pp. 1369–1409, Jul. 2016.
[2] I. A. Hemadeh, K. Satyanarayana, M. El-Hajjar, and L. Hanzo, "Millimeter-wave communications: Physical channel models, design considerations, antenna constructions, and link-budget," *IEEE Commun. Surveys Tuts.*, vol. 20, no. 2, pp. 870–913, 2nd Quart., 2018.
[3] A.-G. Acx and P. Mendribil, "Capacity evaluation of the UTRA FDD and TDD modes," in *Proc. IEEE 49th Veh. Technol. Conf.*, vol. 3, May 1999, pp. 1999–2003.
[4] P. W. C. Chan, E. S. Lo, R. R. Wang, E. K. S. Au, V. K. N. Lau, R. S. Cheng, W. H. Mow, R. D. Murch, and K. B. Letaief, "The evolution path of 4G networks: FDD or TDD?" *IEEE Commun. Mag.*, vol. 44, no. 12, pp. 42–50, Dec. 2006.
[5] M. Jain, J. Choi, T. Kim, D. Bharadia, S. Seth, K. Srinivasan, P. Levis, S. Katti, and P. Sinha, "Practical, real-time, full duplex wireless," in *Proc. 17th Annu. Int. Conf. Mobile Comput. Netw.*, 2001, pp. 301–312.
[6] M. Duarte, C. Dick, and A. Sabharwal, "Experiment-driven characterization of full-duplex wireless systems," *IEEE Trans. Wireless Commun.*, vol. 11, no. 12, pp. 4296–4307, Dec. 2012.
[7] T. Riihonen, S. Werner, and R. Wichman, "Mitigation of loopback self-interference in full-duplex MIMO relays," *IEEE Trans. Signal Process.*, vol. 59, no. 12, pp. 5983–5993, Dec. 2011.
[8] Z. Zhang, X. Chai, K. Long, A. V. Vasilakos, and L. Hanzo, "Full duplex techniques for 5G networks: Self-interference cancellation, protocol design, and relay selection," *IEEE Commun. Mag.*, vol. 53, no. 5, pp. 128–137, May 2015.
[9] A. Sabharwal, P. Schniter, D. Guo, D. W. Bliss, S. Rangarajan, and R. Wichman, "In-band full-duplex wireless: Challenges and opportunities," *IEEE J. Sel. Areas Commun.*, vol. 32, no. 9, pp. 1637–1652, Sep. 2014.
[10] G. Liu, F. R. Yu, H. Ji, V. C. M. Leung, and X. Li, "In-band full-duplex relaying: A survey, research issues and challenges," *IEEE Commun. Surveys Tuts.*, vol. 17, no. 2, pp. 500–524, 2nd Quart., 2015.
[11] D. Kim, H. Lee, and D. Hong, "A survey of in-band full-duplex transmission: From the perspective of PHY and MAC layers," *IEEE Commun. Surveys Tuts.*, vol. 17, no. 4, pp. 2017–2046, 4th quart., 2015.
[12] L.-L. Yang, *Multicarrier Communications*. Hoboken, NJ, USA: Wiley, Jan. 2009.
[13] L.-L. Yang, "Multicarrier-division duplexing (MDD): A duplexing scheme whose time has come," *IEEE COMSOC MMTC E-Lett.*, vol. 10, pp. 35–38, Jan. 2015.

[14] D. Steer, K. Teo, and B. Kirkland, "Novel method for communications using orthogonal division duplexing of signals (ODD)," in *Proc. IEEE 56th Veh. Technol. Conf.*, vol. 1, Sep. 2002, pp. 381–385.

[15] R. Kimura and S. Shimamoto, "A multi-carrier based approach to wireless duplex: Orthogonal frequency division duplex (OFDD)," in *Proc. 3rd Int. Symp. Wireless Commun. Syst.*, Sep. 2006, pp. 368–372.

[16] P. Tarasak and H. Minn, "Resource allocation for multipoint-to-multipoint orthogonal multicarrier division duplexing," in *Proc. IEEE Global Commun. Conf. (GLOBECOM)*, Dec. 2012, pp. 3988–3993.

[17] W. Qiu, P. Tarasak, and H. Minn, "Orthogonal multicarrier division multiple access for multipoint-to-multipoint networks," *IEEE Trans. Commun.*, vol. 61, no. 9, pp. 3841–3853, Sep. 2013.

[18] *User Equipment (UE) Radio Transmission and Reception*, document TS 36.101, 3GPP, 2019. [Online]. Available: http://www.3gpp.org/ftp//Specs/archive/36 series/36.101/

[19] C. A. Balanis, *Antenna Theory: Analysis and Design*, 3rd ed. Hoboken, NJ, USA: Wiley, 2005.

[20] B. S. Krongold and D. L. Jones, "PAR reduction in OFDM via active constellation extension," *IEEE Trans. Broadcast.*, vol. 49, no. 3, pp. 258–268, Sep. 2003.

[21] Y. J. Kou, W. S. Lu, and A. Antoniou, "A new peak-to-average power-ratio reduction algorithm for OFDM systems via constellation extension," *IEEE Trans. Wireless Commun.*, vol. 6, no. 5, pp. 1823–1832, May 2007.

[22] Y. Wang, W. Chen, and C. Tellambura, "Genetic algorithm based nearly optimal peak reduction tone set selection for adaptive amplitude clipping PAPR reduction," *IEEE Trans. Broadcast.*, vol. 58, no. 3, pp. 462–471, Sep. 2012.

[23] S. H. Han and J. H. Lee, "An overview of peak-to-average power ratio reduction techniques for multicarrier transmission," *IEEE Wireless Commun.*, vol. 12, no. 2, pp. 56–65, Apr. 2005.

[24] *NR Physical Channels and Modulation (Release 15)*, document TS 38.211, 3GPP, 2019. [Online]. Available: http://www.3gpp.org/ftp//Specs/archive/38 series/38.211/

[25] R. W. Heath, Jr., N. González-Prelcic, S. Rangan, W. Roh, and A. M. Sayeed, "An overview of signal processing techniques for millimeter wave MIMO systems," *IEEE J. Sel. Topics Signal Process.*, vol. 10, no. 3, pp. 436–453, Apr. 2016.

[26] R. Rajashekar and L. Hanzo, "Hybrid beamforming in mm-Wave MIMO systems having a finite input alphabet," *IEEE Trans. Commun.*, vol. 64, no. 8, pp. 3337–3349, Aug. 2016.

[27] A. Alkhateeb, O. El Ayach, G. Leus, and R. W. Heath, Jr., "Channel estimation and hybrid precoding for millimeter wave cellular systems," *IEEE J. Sel. Topics Signal Process.*, vol. 8, no. 5, pp. 831–846, Oct. 2014.

[28] J. Singh and S. Ramakrishna, "On the feasibility of codebook-based beamforming in millimeter wave systems with multiple antenna arrays," *IEEE Trans. Wireless Commun.*, vol. 14, no. 5, pp. 2670–2683, May 2015.

[29] Z. Xiao, P. Xia, and X.-G. Xia, "Channel estimation and hybrid precoding for millimeter-wave MIMO systems: A low-complexity overall solution," *IEEE Access*, vol. 5, pp. 16100–16110, 2017.

[30] A. Alkhateeb, G. Leus, and R. W. Heath, Jr., "Limited feedback hybrid precoding for multi-user millimeter wave systems," *IEEE Trans. Wireless Commun.*, vol. 14, no. 11, pp. 6481–6494, Nov. 2015.

[31] W. Ni and X. Dong, "Hybrid block diagonalization for massive multiuser MIMO systems," *IEEE Trans. Commun.*, vol. 64, no. 1, pp. 201–211, Jan. 2016.

[32] R. Rajashekar and L. Hanzo, "User selection algorithms for block diagonalization aided multiuser downlink mm-Wave communication," *IEEE Access*, vol. 5, pp. 5760–5772, 2017.

[33] R. Rajashekar and L. Hanzo, "Iterative matrix decomposition aided block diagonalization for mm-Wave multiuser MIMO systems," *IEEE Trans. Wireless Commun.*, vol. 16, no. 3, pp. 1372–1384, Mar. 2017.

[34] Z. Wei, X. Zhu, S. Sun, Y. Huang, L. Dong, and Y. Jiang, "Full-duplex versus half-duplex amplify-and-forward relaying: Which is more energy efficient in 60-GHz dual-hop indoor wireless systems?" *IEEE J. Sel. Areas Commun.*, vol. 33, no. 12, pp. 2936–2947, Dec. 2015.

[35] A. Shojaeifard, K.-K. Wong, M. D. Renzo, G. Zheng, K. A. Hamdi, and J. Tang, "Massive MIMO-enabled full-duplex cellular networks," *IEEE Trans. Commun.*, vol. 65, no. 11, pp. 4734–4750, Nov. 2017.

[36] X. Liu, Z. Xiao, L. Bai, J. Choi, P. Xia, and P.-G. Xia, "Beamforming based full-duplex for millimeter-wave communication," *Sensors*, vol. 16, no. 7, p. 1130, 2016.

[37] Z. Xiao, P. Xia, and X.-G. Xia, "Full-duplex millimeter-wave communication," *IEEE Wireless Commun.*, vol. 24, no. 6, pp. 136–143, Dec. 2017.

[38] Z. Xiao, X. G. Xia, D. Jin, and N. Ge, "Iterative eigenvalue decomposition and multipath-grouping Tx/Rx joint beamformings for millimeter-wave communications," *IEEE Trans. Wireless Commun.*, vol. 14, no. 3, pp. 1595–1607, Mar. 2015.

[39] *Study on Channel Model for Frequencies from 0.5 to 100 GHz (Release 15)*, document TS 38.901, 3GPP, 2019. [Online]. Available: http://www.3gpp.org/ftp//Specs/archive/38 series/38.901/

[40] S. Sun, T. S. Rappaport, R. W. Heath, Jr., A. Nix, and S. Rangan, "MIMO for millimeter-wave wireless communications: Beamforming, spatial multiplexing, or both?" *IEEE Commun. Mag.*, vol. 52, no. 12, pp. 110–121, Dec. 2014.

[41] A. J. Fenn, "Evaluation of adaptive phased array antenna, far-field nulling performance in the near-field region," *IEEE Trans. Antennas Propag.*, vol. 38, no. 2, pp. 173–185, Feb. 1990.

[42] A. D. Yaghjian, "An overview of near-field antenna measurements," *IEEE Trans. Antennas Propag.*, vol. AP-34, no. 1, pp. 30–45, Jan. 1986.

[43] A. E. Sayers, W. M. Dorsey, K. W. O'Haver, and J. A. Valenzi, "Planar near-field measurement of digital phased arrays using near-field scan plane reconstruction," *IEEE Trans. Antennas Propag.*, vol. 60, no. 6, pp. 2711–2718, Jun. 2012.

[44] N. P. Lawrence, B. W.-H. Ng, H. J. Hansen, and D. Abbott. *Analysis of Millimetre-Wave Polarization Diverse Multiple-Input Multiple-Output Capacity*. Accessed: 2015. [Online]. Available: https://royalsocietypublishing.org/doi/10.1098/rsos.150322

[45] F. H. Raab, P. Asbeck, S. Cripps, P. B. Kenington, Z. B. Popovic, N. Pothecary, J. F. Sevic, and N. O. Sokal, "Power amplifiers and transmitters for RF and microwave," *IEEE Trans. Microw. Theory Techn.*, vol. 50, no. 3, pp. 814–826, Mar. 2002.

[46] J. Joung, C. K. Ho, K. Adachi, and S. Sun, "A survey on power-amplifier-centric techniques for spectrum- and energy-efficient wireless communications," *IEEE Commun. Surveys Tuts.*, vol. 17, no. 1, pp. 315–333, 1st Quart., 2015.

[47] C. Xu, T. Bai, J. Zhang, R. G. Maunder, S. Sugiura, Z. Wang, and L. Hanzo, "Constant-envelope space-time shift keying," *IEEE J. Sel. Topics Signal Process.*, to be published.

[48] T. S. Rappaport, Y. Xing, O. Kanhere, S. Ju, A. Madanayake, S. Mandal, A. Alkhateeb, and G. C. Trichopoulos, "Wireless communications and applications above 100 GHz: Opportunities and challenges for 6G and beyond," *IEEE Access*, vol. 7, pp. 78729–78757, 2019.

[49] A.-A. A. Boulogeorgos, A. Alexiou, T. Merkle, C. Schubert, R. Elschner, A. Katsiotis, P. Stavrianos, D. Kritharidis, P. Chartsias, J. Kokkoniemi, M. Juntti, J. Lehtomaki, A. Teixeira, and F. Rodrigues, "Terahertz technologies to deliver optical network quality of experience in wireless systems beyond 5G," *IEEE Commun. Mag.*, vol. 56, no. 6, pp. 144–151, Jun. 2018.

[50] C. Lin and G. Y. Li, "Terahertz communications: An array-of-subarrays solution," *IEEE Commun. Mag.*, vol. 54, no. 12, pp. 124–131, Dec. 2016.

[51] I. F. Akyildiz, J. M. Jornet, and C. Han, "Terahertz band: Next frontier for wireless communications," *Phys. Commun.*, vol. 12, pp. 16–32, Sep. 2014.

[52] P. Y. Chen, C. Argyropoulos, and A. Alù, "Terahertz antenna phase shifters using integrally-gated graphene transmission-lines," *IEEE Trans. Antennas Propag.*, vol. 61, no. 4, pp. 1528–1537, Apr. 2013.

[53] P. K. Frenger and N. A. B. Svensson, "Parallel combinatory OFDM signaling," *IEEE Trans. Commun.*, vol. 47, no. 4, pp. 558–567, Apr. 1999.

[54] D. Tsonev, S. Sinanovic, and H. Haas, "Enhanced subcarrier index modulation (SIM) OFDM," in *Proc. IEEE GLOBECOM Workshops*, Dec. 2011, pp. 728–732.

[55] C. Xu, S. Sugiura, S. X. Ng, P. Zhang, L. Wang, and L. Hanzo, "Two decades of MIMO design tradeoffs and reduced-complexity MIMO detection in near-capacity systems," *IEEE Access*, vol. 5, pp. 18564–18632, 2017.

[56] T. Jiang and Y. Wu, "An overview: Peak-to-average power ratio reduction techniques for OFDM signals," *IEEE Trans. Broadcast.*, vol. 54, no. 2, pp. 257–268, Jun. 2008.

[57] D. Tsonev, S. Sinanovic, and H. Haas, "Complete modeling of nonlinear distortion in OFDM-based optical wireless communication," *J. Lightw. Technol.*, vol. 31, no. 18, pp. 3064–3076, Sep. 15, 2013.

[58] T. Mao, Z. Wang, Q. Wang, S. Chen, and L. Hanzo, "Dual-mode index modulation aided OFDM," *IEEE Access*, vol. 5, pp. 50–60, 2017.

[59] E. Basar, M. Wen, R. Mesleh, M. Di Renzo, Y. Xiao, and H. Haas, "Index modulation techniques for next-generation wireless networks," *IEEE Access*, vol. 5, pp. 16693–16746, 2017.

[60] M. Heino, D. Korpi, T. Huusari, E. Antonio-Rodriguez, S. Venkatasubramanian, T. Riihonen, L. Anttila, C. Icheln, K. Haneda, R. Wichman, and M. Valkama, "Recent advances in antenna design and interference cancellation algorithms for in-band full duplex relays," *IEEE Commun. Mag.*, vol. 53, no. 5, pp. 91–101, May 2015.
[61] R. A. Horn and C. R. Johnson, *Matrix Analysis*, 2nd ed. Cambridge, U.K.: Cambridge Univ. Press, 2013.

RAKSHITH RAJASHEKAR (M'14–SM'17) received the B.E. degree in electrical communication engineering from Visvesvaraya Technological University, Karnataka, India, in 2007, and the Ph.D. degree from the Department of Electrical Communication Engineering, Indian Institute of Science (IISc), India, in 2014. He was with Accord Software & Systems, Bengaluru, India, as a Systems Engineer, from 2007 to 2009, and as a Senior Scientist with Broadcom Communications, Bengaluru, from 2014 to 2015. He is currently a Research Fellow with the University of Southampton, U.K. His research interests include antenna selection in MIMO systems, differential communication, millimeter-wave communication, and communication between drones with a focus on space–time signal processing and coding. He was a recipient of the Special Recognition Award from Broadcom Communications, India, and the Dean's Award from the University of Southampton, U.K., for excellence in research. He has received the Best Reviewer award from the IEEE TRANSACTIONS ON WIRELESS COMMUNICATIONS, the IEEE TRANSACTIONS ON COMMUNICATIONS, and the IEEE WIRELESS COMMUNICATIONS LETTERS.

CHAO XU (S'09–M'14) received the B.Eng. degree in telecommunications engineering with management from the Beijing University of Posts and Telecommunications, China, the B.Sc. (Eng.) degree (Hons.) in telecommunications engineering with management from the Queen Mary, University of London, U.K., through a Sino-U.K. Joint Degree Program, in 2008, and the M.Sc. degree (Hons.) in radio-frequency communication systems and the Ph.D. degree in wireless communications from the University of Southampton, U.K., in 2009 and 2015, respectively, where he is currently a Postdoctoral Researcher with the Next Generation Wireless Research Group. His research interests include index modulation, reduced-complexity MIMO design, noncoherent detection, and turbo detection. He received the Best M.Sc. Student Award in Broadband and Mobile Communication Networks from the IEEE Communications Society (U.K. and Ireland Chapter), in 2009. He also received the 2012 Chinese Government Award for Outstanding Self-Financed Student Abroad.

NAOKI ISHIKAWA (S'13–M'17) was born in Kanagawa, Japan, in 1991. He received the B.E., M.E., and Ph.D. degrees from the Tokyo University of Agriculture and Technology, Tokyo, Japan, in 2014, 2015, and 2017, respectively.

From June 2015 to September 2015, he was an Academic Visitor with the School of Electronics and Computer Science, University of Southampton, U.K. From April 2016 to March 2017, he was a Research Fellow of the Japan Society for the Promotion of Science. Since April 2017, he has been an Assistant Professor with the Graduate School of Information Sciences, Hiroshima City University, Japan. He was certified as an Exemplary Reviewer of the IEEE TRANSACTIONS ON COMMUNICATIONS, in 2017. He also received eight domestic awards, including the Yasujiro Niwa Outstanding Paper Award from Tokyo Denki University, in 2018, the Telecom System Technology Student Award (honorable mention) from the Telecommunications Advancement Foundation of Japan, in 2014, and the Outstanding Paper Award for Young C&C Researchers from the NEC C&C Foundation, in 2014.

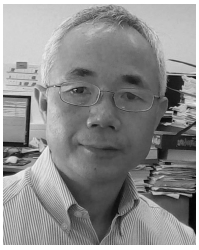

LIE-LIANG YANG (M'98–SM'02–F'16) received the B.Eng. degree in communications engineering from Shanghai Tiedao University, Shanghai, China, in 1988, and the M.Eng. and Ph.D. degrees in communications and electronics from Northern (Beijing) Jiaotong University, Beijing, China, in 1991 and 1997, respectively. From June 1997 to December 1997, he was a Visiting Scientist with the Institute of Radio Engineering and Electronics, Academy of Sciences of the Czech Republic. Since December 1997, he has been with the University of Southampton, U.K., where he is currently a Professor of wireless communications with the School of Electronics and Computer Science. He has published over 360 research papers in journals and conference proceedings, has authored/coauthored three books, and has also published several book chapters. His research interests include wireless communications, wireless networks and signal processing for wireless communications, and molecular communications and nano-networks. The details about his research publications can be found at http://www.mobile.ecs.soton.ac.uk/lly/. He is a Fellow of the IET and a Distinguished Lecturer of the IEEE. He served as an Associate Editor for the IEEE TRANSACTIONS ON VEHICULAR TECHNOLOGY and the *Journal of Communications and Networks* (JCN) and is currently an Associate Editor of IEEE ACCESS and the *Security and Communication Networks* (SCN) journal.

LAJOS HANZO (M'91–SM'92–F'04) received the D.Sc. degree in electronics and the Ph.D. degree, in 1976 and 1983, respectively. During his 40-year career in telecommunications, he has held various research and academic posts in Hungary, Germany, and U.K. Since 1986, he has been with the School of Electronics and Computer Science, University of Southampton, U.K., where he is currently the Chair in telecommunications. From 2008 to 2012, he was a Chaired Professor at Tsinghua University, Beijing. He has successfully supervised 100 Ph.D. students, has coauthored 20 John Wiley/IEEE Press books on mobile radio communications totaling in excess of 10 000 pages, has published over 1800 research contributions at the IEEE Xplore, has acted both as the TPC and General Chair of IEEE conferences, has presented keynote lectures, and has been received a number of distinctions. He is currently directing an Academic Research Team, working on a range of research projects in the field of wireless multimedia communications sponsored by industry, the Engineering and Physical Sciences Research Council (EPSRC), U.K., the European Research Council's Advanced Fellow Grant, and the Royal Society's Wolfson Research Merit Award. His research was funded by the European Research Council's Senior Research Fellow Grant. He is an Enthusiastic Supporter of Industrial and Academic Liaison, and he offers a range of industrial courses. He is a Fellow of the Royal Academy of Engineering, IET, and EURASIP. In 2009, he received an Honorary Doctorate from the Technical University of Budapest and, in 2015, from The University of Edinburgh. He is also a Governor of the IEEE VTS. From 2008 to 2012, he was the Editor-in-Chief of the IEEE Press. For further information on research in progress and associated publications, please refer to http://www-mobile.ecs.soton.ac.uk.